ISSN 0957-4484

NANOTECHNOLOGY

VOLUME 28 NUMBER 22 2 JUNE 2017

Nanotechnology

Vol 28, No 22 224001–225704

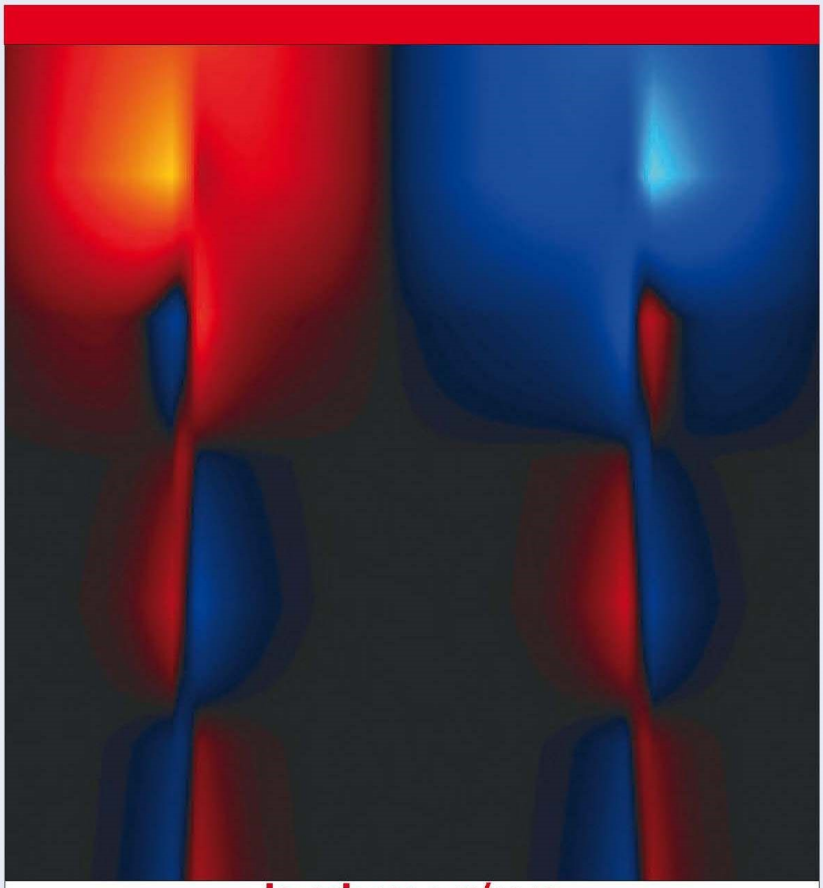

iopscience.org/nano

Featured article

Maskless fabrication of slanted annular aperture arrays

Jiangtao Lv, Eng Huat Khoo, Eunice Sok Ping Leong, Litao Hu, Xiaoxiao Jiang, Yong Li, Dan Luo, Guangyuan Si and Yan Jun Liu

2 June 2017

IOP Publishing

IOP Publishing Nanotechnology
Nanotechnology 28 (2017) 225302 (7pp) https://doi.org/10.1088/1361-6528/aa6c95

Maskless fabrication of slanted annular aperture arrays

Jiangtao Lv[1], Eng Huat Khoo[2], Eunice Sok Ping Leong[3], Litao Hu[4], Xiaoxiao Jiang[1], Yong Li[4], Dan Luo[4], Guangyuan Si[1,5] and Yan Jun Liu[4,5]

[1] College of Information Science and Engineering, Northeastern University, Shenyang 110004, People's Republic of China
[2] Institute of High Performance Computing, Agency for Science, Technology and Research (A*STAR), 1 Fusionopolis Way, Connexis, #16-16, Singapore 138632, Singapore
[3] Institute of Materials Research and Engineering, Agency for Science, Technology and Research (A*STAR), 2 Fusionopolis Way, Innovis, #08-03, Singapore 138634, Singapore
[4] Department of Electrical and Electronic Engineering, Southern University of Science and Technology, Shenzhen 518055, People's Republic of China

E-mail: siguang0323@hotmail.com and yjliu@sustc.edu.cn

Received 11 March 2017
Accepted for publication 11 April 2017
Published 10 May 2017

Abstract

We report maskless fabrication of high-aspect-ratio slanted annular aperture arrays (SAAAs) in gold films using focused ion beam lithography. By tilting the substrate, SAAAs with the desired tilting angle can be fabricated. Our experimental results demonstrate accurate control over aperture size, obliqueness, and reproducibility. We also show that the resulted plasmonic resonances of SAAAs can be effectively tuned via obliqueness control. This versatile approach may enable fabrication of more complicated plasmonic nanostructures. The demonstrated gold SAAAs could also find many potential applications in plasmon-assisted sensing and surface enhanced spectroscopy.

Keywords: annular aperture array, plasmonic resonance, nanofabrication

(Some figures may appear in colour only in the online journal)

1. Introduction

Slanted micro-/nanostructures on a flat surface have found many unique applications due to their structure-enabled directional and anisotropic surface properties [1]. For example, artificially designed surfaces that mimick gecko feet have unidirectional frictional force for dry adhesive pads application [2, 3]; unidirectional liquid wetting/spreading has also been demonstrated through a slanted nanostructured surface [4, 5], which enables a variety of applications involving biomedical devices and sensors [6]. Given the huge potential for various applications, fabrication of slanted micro-/nanostructures has been extensively studied. Microscale slanted structures can be readily fabricated using contact or proximity photolithography by tilting the substrates [7, 8], while nanoscale ones have been fabricated by reactive ion etching with tilted substrates and modification of the etching system (i.e., the addition of a Faraday cage to control the ion incident angles) [9]. Glancing angle deposition (GLAD) can be also used to create slanted pillars but it lacks accurate control of the pillar spacing or diameter [10]. Kustandi *et al* have demonstrated synthetic butterfly wings with slanted polymer nanostructure using combined nanoimprinting lithography and shear patterning technique [11]. To achieve much higher accuracy and resolution for the slanted structures, electron-beam lithography appears as the best option. Zhang *et al* have demonstrated periodic tilted nanostructures by making use of the dynamic focus function that is available for most scanning electron microscopy systems [12].

Recently, slanted plasmonic (i.e., those noble metals, such as Au, Ag, or Al) nanostructures have attracted increasing attention since they can produce unusual optical properties that can be used to mold the light propagation. For example, Verre *et al* have demonstrated that a metasurface of

[5] Authors to whom any correspondence should be addressed.

slanted gold nanopillar array can enable directional light extinction and emission [13], which results from a tilted dipolar oscillation in each individual nanopillar with respect to the sample normal. Kim *et al* have reported that a slanted nanoaperture array on a metal surface demonstrates anomalous refraction of light for a wide range of incident angles [14]. Baida *et al* have theoretically investigated enhanced transmission properties of a slanted annular aperture array (SAAA) due to the peculiar excitation of the cutoff-free transverse electromagnetic (TEM) guided mode [15–17]. Though Ndao and coworkers have demonstrated SAAA fabrication [18], the obtained results still appear as preliminary with a perceived lack of controllability. As a result, it is still very challenging to fabricate slanted metallic nanostructures. The main limit of the above mentioned approaches is that only 2D periodic structures with simple geometries and low aspect ratios can be fabricated, such as pillars or holes. Moreover, most slanted structures are limited to dielectric materials. Therefore, it is highly desirable to have an effective technique to fabricate plasmonic structures with arbitrary geometries.

Focused ion beam (FIB) lithography is a maskless, versatile technique that can be used to directly mill the designed structure with high resolution at the nanoscale. Compared to other nanofabrication techniques, such as electron-beam lithography and reactive ion etching, FIB is much more competitive in fabricating nanostructures with high aspect ratios. We have successfully demonstrated the fabrication of dense nanostructure arrays using FIB in both dielectric and metallic materials [19–22]. However, high-aspect-ratio slanted nanostructures on flat substrates have not been studied using the FIB technique. In this work, we report maskless fabrication of high-aspect-ratio SAAAs in gold films using FIB lithography. By simply tilting the substrate, SAAAs with different tilting angles are achieved. The FIB lithography provides accurate control over aperture size, obliqueness, and reproducibility. Experimental results show that the plasmonic resonances of SAAAs can be effectively tuned via obliqueness control. Much more complicated SAAA-based hierarchical or three-dimensional plasmonic nanostructures could be fabricated using this versatile technique. The demonstrated gold SAAAs could possibly be applied in refractive index sensing [23–25] and surface-enhanced Raman scattering (SERS) [26–28] applications.

2. Experimental and simulations

2.1. Fabrication

360 nm thick gold films were deposited on quartz substrates with an adhesion layer of 10 nm titanium in between using electron-beam evaporation (Edwards Auto306). To control the surface roughness introduced by evaporation, a low deposition rate ($\sim$0.04 nm s^{-1}) was employed. A single-beam FIB system (FEI Corporation, FIB 200) was used to define the SAAA structures in this work. One should note that the profile of the milled SAAA can significantly affect the optical response.

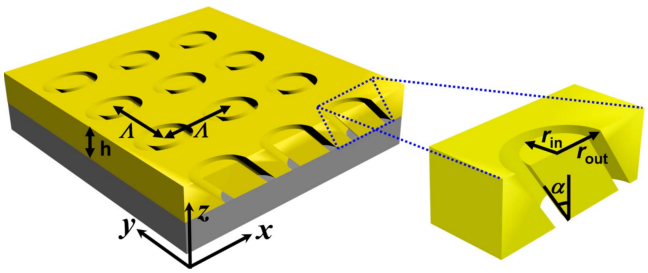

Figure 1. Geometrical design of gold SAAA with important structural parameters.

Several milling variables should be tuned carefully and precisely to achieve accurate control on the profile of SAAAs, e.g. dwelling time, overlap of the ion beam and etching duration. To minimize the redeposition effects during FIB milling, all arrays were milled in parallel. During FIB milling, 70 pA beam current was selected with an accelerating voltage of 30 kV. More details can be found elsewhere [21, 29].

2.2. Characterization

The surface morphologies of SAAAs were characterized using scanning electron microscopy (SEM). To observe the cross-sectional morphologies of SAAAs, the SAAA was cut by FIB and then observed by SEM. To characterize the optical properties of fabricated structures, a UV-Visible-NIR microspectrometer (CRAIC QDI 2010™) with a 75 W broadband xenon source was used. The incident broadband light was focused to have a detecting area of 7.1 $\times$ 7.1 μm^2 using a 36$\times$ objective lens combined with a variable aperture. Reflectivity measurements were normalized to the reflectance of an aluminium mirror.

2.3. Simulation

The simulation of SAAAs was carried out using a finite-difference time-domain (FDTD) method with commercial software (Lumerical). Non-uniform meshes in the range of 2 nm to 5 nm were applied to the slanted nanostructure. The smaller mesh was applied to the slanted region, while the larger mesh in the bulk gold and quartz region. In the z-direction, the mesh size was 4 nm. The periodic boundary condition was applied to enable the simulation of the slanted nanostructure in a unit cell in the planar x- and y-direction. The period of the unit cell was 800 nm. In the z-direction, the perfectly matched layer was applied. Unpolarized light was incident onto the nanostructure. The transmission and reflection coefficients were obtained for the SAAA nanostructures. The light dispersion properties of the gold and quartz material were obtained from the Palik optical handbook [30]. The near-field electric-field distributions of the SAAAs were also calculated for both surface and cross-section of the structures.

3. Results and discussion

Figure 1 shows the geometry of the designed gold SAAA. It has a square pattern with a period of Λ in both x- and y-directions.

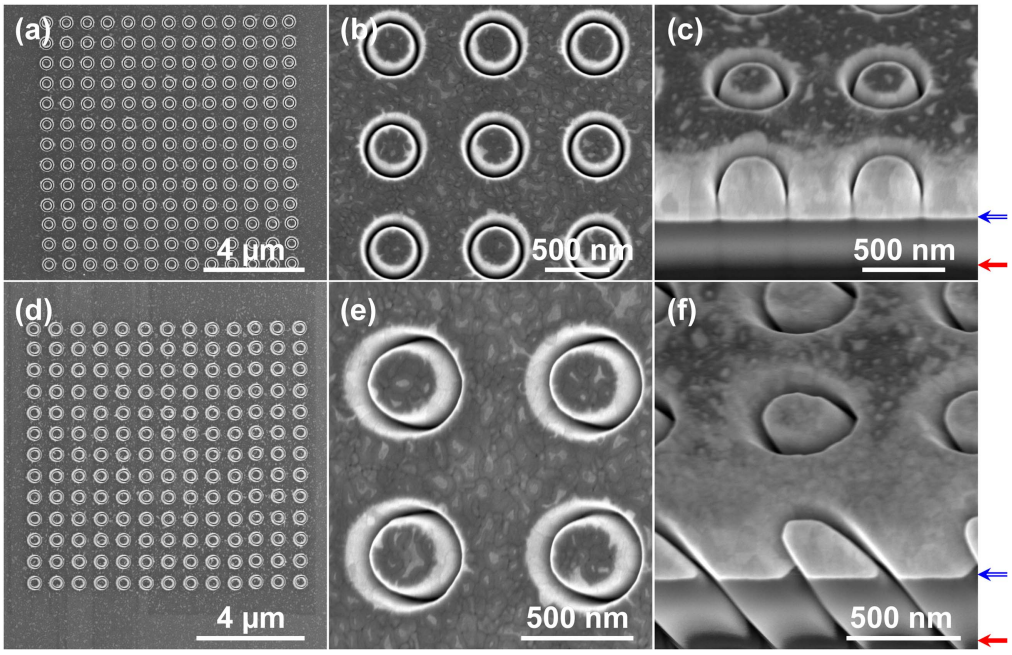

Figure 2. Typical SEM images of two SAAAs with the tilting angles of 0° (a)–(c) and 40° (d)–(f), respectively, illustrating the overview (a), (d), high-magnification top-view (b), (e) and cross-sectional (c), (f) morphologies of the fabricated samples. The red arrows label the interface between gold and quartz substrate.

The inner and outer radii of each individual aperture are labeled as r_{in} and r_{out}, respectively. Each aperture has a tilting angle labeled as α. The deposited gold film thickness, h, is 360 nm. In our experiment, we have milled a series of SAAAs with variable tilting angles using FIB. Figures 2(a)–(e) represent the typical SEM images of two SAAAs, exhibiting excellent reproducibility and uniformness over the fabricated area. The nominal periodicities in both x- and y-directions are 800 nm, and the inner and outer radii of each individual aperture are 200 and 215 nm, respectively. Detailed analyses from the high-magnification SEM images show that the gold film thickness is 360 ± 20 nm and the surface roughness of the gold film is $\sim\pm 10$ nm; the measured geometric parameters of the fabricated samples are very close to the designed values, with a typical deviation within ± 30 nm. A high resolution SEM image also shows the cross-sectional view of these two SAAAs, as shown figures 2(c) and (e). It can be clearly observed that the annular apertures have been completely milled through the gold film. From the SEM images, the aspect ratio of the annular aperture is estimated to be at least ~10:1, which is usually very challenging to achieve for EBL and other lithographic techniques [31–33]. The cross-sectional SEM image shows a clear interface between gold and quartz substrate, which is indicated by the red arrow. We also note that there is another obvious interface indicated by the blue arrow, which is due to the re-deposition or phantom etching during the milling process. From figures 2(c) and (f), we can see that the inner and outer radii vary with the vertical position along the metal thickness, which causes a nonuniform opening aperture from the top to the bottom surface. This is a well-known effect of the FIB technique that allows conical shapes instead of regular vertical edges [19]. In addition, it is worth noting that during the FIB milling of the apertures, the substrate was also partly engraved, which may affect the optical properties of SAAA. This might be one of origins of the discrepancy between theoretical and experimental results, since the substrate engraving was ignored in our simulation.

Figure 3 shows the measured and simulated reflectance spectra of the SAAAs with gradually changed tilting angles and their corresponding SEM images. Overall, the spectral profiles of simulations and experiments are in reasonably good agreement in the spectral range of interest. From figures 3(a) and (b), we can clearly see that there are three distinct dips on the reflectance spectra, denoting different plasmonic resonance modes (M-I, M-II, and M-III). These resonance modes follow a similar trend, and all red-shift as the tilting angle increases. Also, the reflected intensity gradually reduces for structures characterized by increasing the tilting angle from 0° to 40°.

The three different resonance modes observed can be mainly attributed to coherent interactions between two types of plasmons: cylindrical surface plasmons (CSPs) and planar surface plasmons (PSPs). CSPs strongly depend on the geometry and the thickness of the AAA structure, while PSPs are closely related to the lateral period of the AAA structure. Our AAA structure is equivalent to the superposition of a two-dimensional gratings and a finite annular waveguide array. In our design, the annular apertures with a finite length can serve as a waveguide, which also forms opened Fabry–Pérot cavities as the generated CSPs propagate inside the annular aperture and experience multiple reflections at both end-facets. As a result, the CSP-induced reflectance dip is a direct result of the Fabry–Pérot resonances. The CSP excitation has to satisfy the following resonance condition [34],

$$|2Lk_{SPP}(\omega) + \Delta\phi_1 + \Delta\phi_2| = 2m\pi \qquad (1)$$

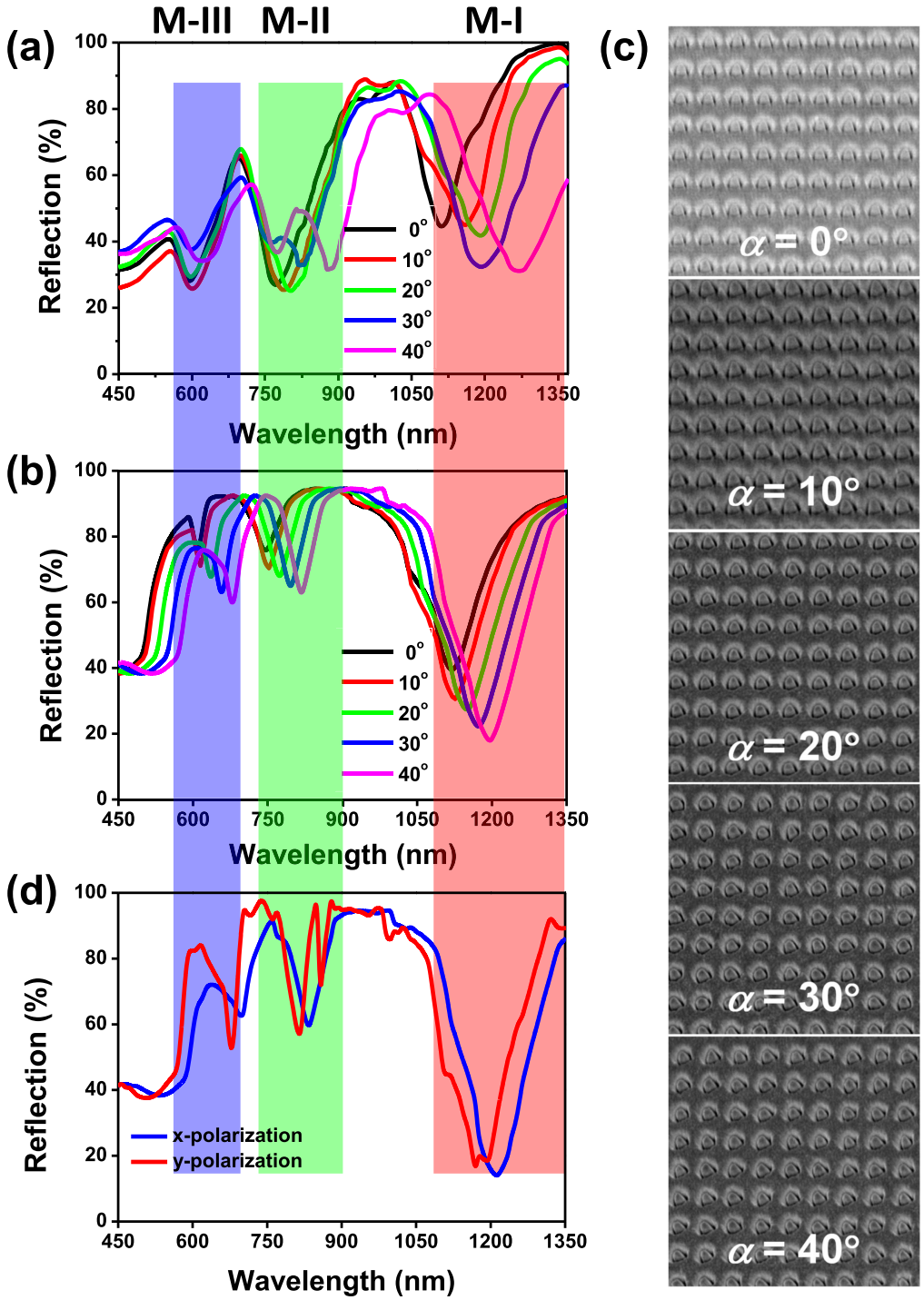

Figure 3. Experimentally measured (a) and simulated (b) reflection spectra, and corresponding SEM images (c) of the SAAAs with different tilting angles. (d) Simulated reflection spectra of the SAAA at $\alpha = 40°$ for incident light with both *x*- and *y*-polarizations by considering the structural anisotropy. Three distinct reflection dips representing different plasmonic resonance modes on the reflectance spectra are labelled as M-I, M-II, and M-III, respectively.

where L is the length of the Fabry–Pérot cavity, $k_{SPP}(\omega)$ is the wave vector of the CSP at frequency of ω, $\Delta\phi_{1,2}$ is the phase shift as a result of CSP reflection at either facet of the cavity, and m is the mode number. The PSP-induced resonance modes can be written as [35],

$$\lambda_{\max} = (\Lambda/\sqrt{n_x^2 + n_y^2})\sqrt{\varepsilon_d \varepsilon_m/(\varepsilon_d + \varepsilon_m)} \qquad (2)$$

where ε_d and ε_m are the dielectric functions of the dielectric and the metal, respectively, Λ is the lattice constant of the array, and n_x and n_y are integers. In our case, the observed reflection dips (M-I) in the range of 1100–1280 nm in figure 3(a) can be attributed to the CSP excitation. The observed reflection dips (M-II) in the range of 760–900 nm satisfy the above expression for a $\pm(1, 1)$ mode at the Au/air

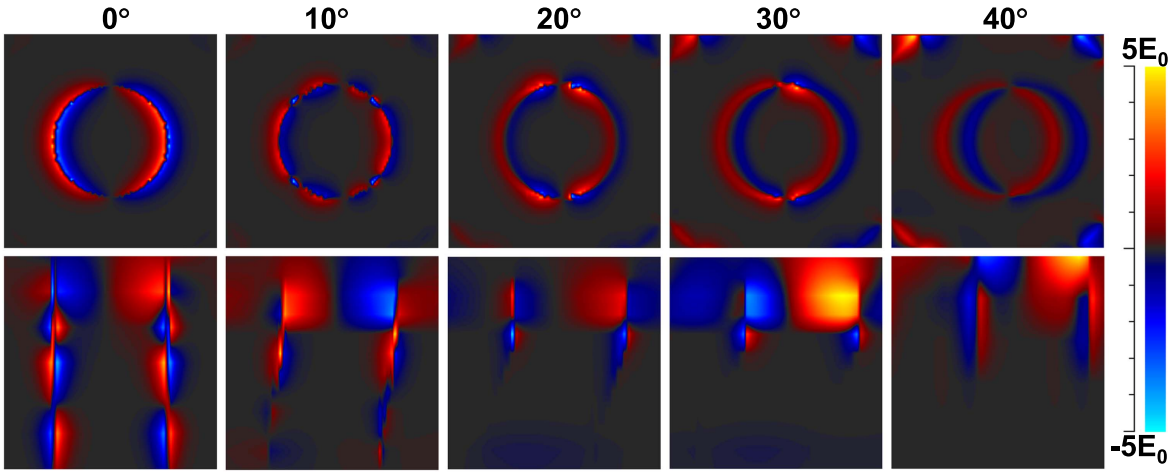

Figure 4. Calculated near-field electric-field distributions for the plasmonic mode M-I of SAAAs with different tilting angles including both top (upper row) and cross-sectional (lower row) views.

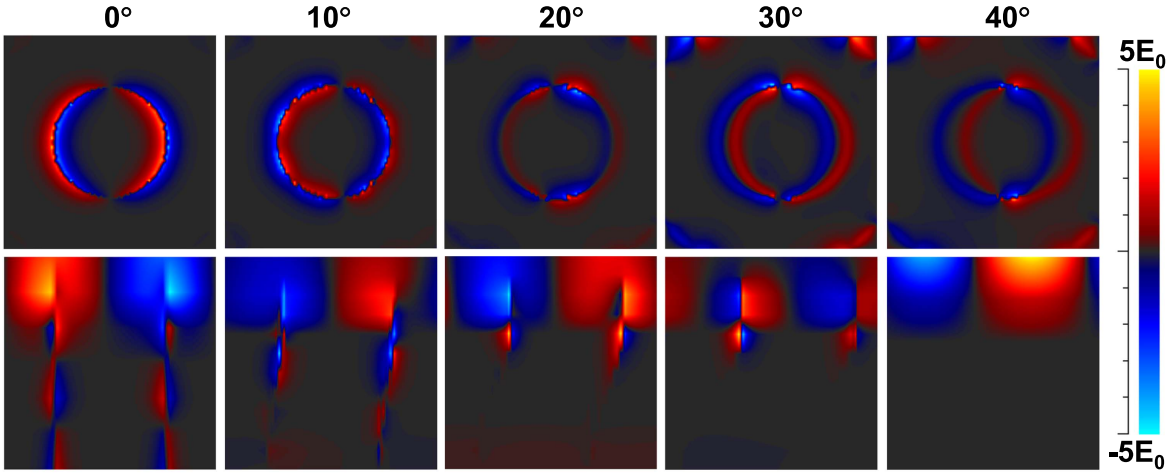

Figure 5. Calculated near-field electric-field distributions for the plasmonic mode M-II of SAAAs with different tilting angles including both top (upper row) and cross-sectional (lower row) views.

interface, while the ones (M-III) in the range of 580–630 nm correspond to either an $\pm(0, 1)$ or $\pm(1, 0)$ mode.

It is worth mentioning that there are some discrepancies between the experimental and simulation results. It is particularly interesting to note that for M-II, it is also remarkable that the reflection dips for 30° and 40° are split into two clear dips, respectively. We attribute this split to the structural anisotropy due to the oblique milling. It can be clearly seen from figure 2(b) that the structure is isotropic at $\alpha = 0°$. As the tilting angle increases, the annular aperture becomes anisotropic. It is particularly obvious when the tilting angle is large, as shown in figure 2(d). This in-plane structural anisotropy will then cause the polarization non-degeneracy of the plasmonic resonance state, resulting in a split of the reflection dip. Figure 3(d) shows the simulated reflection spectra of SAAA at $\alpha = 40°$ by considering the in-plane structural anisotropy. It is clearly seen that there is a dip split for the incident *y*-polarized light, which further confirmed our speculations by the simulation results. Meanwhile for M-I and M-III, the experimental results do not follow our simulations well. For example, the reflection dips for 20° and 30° are experimentally in the same position (∼1200 nm) in M-I. The experimental reflection dips in M-III do not have a monotonical trend compared to the simulation results. In addition, for all the resonance modes, the experimentally observed dips are much more broad and blue-shifted. The experimentally measured reflection for M-II and M-III is much lower than the simulated counterpart. All these observed differences can be mainly attributed to multiple factors, such as the fabrication errors/imperfections, the shape tolerance of designed structures, re-deposition effect during FIB milling process, damping effect of the adhesion layer, and the refractive index difference (including both real and imaginary parts) between simulations and experiments.

To further confirm the origin of these modes, the near-field electric-field distributions were also calculated at their reflectance dips, as shown in figures 4–6. It is clear from the top views in figures 4–6 that the resonance modes M-I and M-II result from the dipolar plasmon resonance mode, while

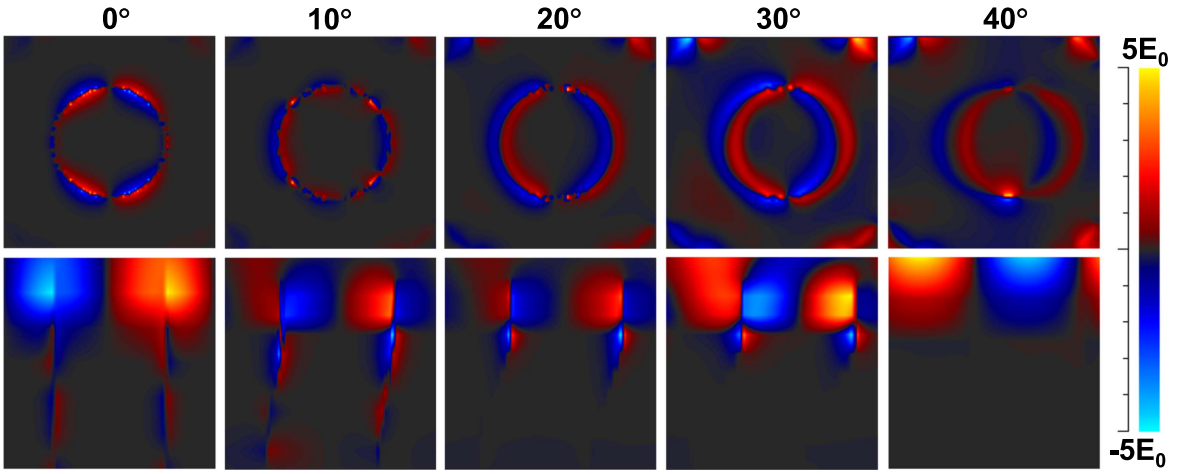

Figure 6. Calculated near-field electric-field distributions for the plasmonic mode M-III of SAAAs with different tilting angles including both top (upper row) and cross-sectional (lower row) views.

the resonance mode M-III comes from the quadrupolar plasmon resonance mode. At the resonance modes, the free electrical charges at the inner rod and outer aperture inside one unit annular aperture form a dipole oscillation respectively and then couple each other, resulting in different electric-field distributions that correspond observed resonance modes as shown in figures 4–6. We can also see that as the tilting angle increases, the opening of the aperture becomes slightly larger. As a result, the spatial distribution of the dipolar resonance becomes broader. It is worth noting that when the tilting angle increases, the quadrupolar plasmon resonance mode degenerates into a dipolar one. It can be also observed from the cross-sectional views in figures 4–6 that the Fabry–Pérot resonances of CSP are formed in the co-axial cavities, which can be clearly confirmed from the non-slanted case. At the resonant mode, there exists a nearly symmetric field distribution inside the aperture and hence significant electric field intensity will transmit through the aperture to the other side of the gold film. As a result, we observed a clear reflection dip from the reflection spectra. We can also see that the Fabry–Pérot resonances become weak as the resonance wavelength shifts blue. As the tilting angle increases, the Fabry–Pérot resonance effect also becomes gradually weaker. The light energy will then be mainly concentrated at the surface.

4. Conclusion

In summary, we have successfully demonstrated high-aspect-ratio gold SAAA fabrication using FIB lithography. By accurately controlling the obliqueness of the FIB cuts, the plasmonic resonances of the SAAAs can be continuously tuned in the interested wavelength range, which offers a great freedom to design the SAAAs with the desired plasmonic resonance wavelength. This versatile approach could also enable fabrication of more complicated plasmonic nanostructures and devices. The demonstrated gold SAAAs could find many potential applications in plasmon-assisted refractive index sensing and SERS spectroscopy.

Acknowledgments

We acknowledge the financial support from the Joint Council Office (JCO) of the Agency for Science Technology and Research (A*STAR) (Grant No. 12302FG012) and the National Natural Science Foundation of China (Grant No. 61405031).

References

[1] Hancock M J, Sekeroglu K and Demirel M C 2012 *Adv. Funct. Mater.* **22** 2223–34
[2] Boesel L F, Greiner C, Arzt E and del Campo A 2010 *Adv. Mater.* **22** 2125–37
[3] Sahay R, Low H Y, Baji A, Foong S and Wood K L 2015 *RSC Adv.* **5** 50821–32
[4] Chu K-H, Xiao R and Wang E N 2010 *Nat. Mater.* **9** 413–7
[5] Malvadkar N A, Hancock M J, Sekeroglu K, Dressick W J and Demirel M C 2010 *Nat. Mater.* **9** 1023–8
[6] Xia D, Johnson L M and López G P 2012 *Adv. Mater.* **24** 1287–302
[7] Aksak B, Murphy M P and Sitti M 2007 *Langmuir* **23** 3322–32
[8] del Campo A and Greiner C 2007 *J. Micromech. Microeng.* **17** R81–95
[9] Jeong H E, Lee J K, Kim H N, Moon S H and Suh K Y 2009 *Proc. Natl Acad. Sci. USA* **106** 5639–44
[10] Hawkeye M M and Brett M J 2007 *J. Vac. Sci. Technol.* A **25** 1317–35
[11] Kustandi T S, Low H Y, Teng J H, Rodriguez I and Yin R 2009 *Small* **5** 574–8
[12] Zhang J, Shokouhi B and Cui B 2012 *J. Vac. Sci. Technol.* B **30** 06F302
[13] Verre R, Svedendahl M, Länk N O, Yang Z J, Zengin G, Antosiewicz T J and Käll M 2016 *Nano Lett.* **16** 98–104
[14] Kim M, Jung Y S, Xi Y and Kim H K 2015 *Appl. Phys. Lett.* **107** 101107
[15] Baida F, Belkhir A, Arar O, Barakat E H, Dahdah J, Chemrouk C, Van Labeke D, Diebold C, Perry N and Bernal M-P 2010 *Micron* **41** 742–5
[16] Baida F I 2007 *Appl. Phys.* B **89** 145–9

[17] Alaridhee T, Ndao A, Bernal M-P, Popov E, Fehrembach A-L and Baida F I 2015 *Opt. Express* **23** 11687–701
[18] Ndao A, Belkhir A, Salut R and Baida F I 2013 *Appl. Phys. Lett.* **103** 211901
[19] Si G Y, Danner A J, Teo S L, Teo E J, Teng J H and Bettiol A A 2011 *J. Vac. Sci. Technol.* B **29** 021205
[20] Liu Y J, Si G Y, Leong E S P, Xiang N, Danner A J and Teng J H 2012 *Adv. Mater.* **24** OP131–5
[21] Si G Y, Zhao Y H, Lv J T, Wang F W, Liu H L, Teng J H and Liu Y J 2013 *Nanoscale* **5** 4309–13
[22] Liu H L, Wang Z L, Huang J, Liu Y J, Fan H J, Zheludev N I and Soci C 2014 *Nano Lett.* **14** 5162–9
[23] Zheng Y B, Juluri B K, Mao X, Walker T R and Huang T J 2008 *J. Appl. Phys.* **103** 014308
[24] Cai Z Y, Liu Y J, Lu X M and Teng J H 2013 *J. Phys. Chem.* C **117** 9440–5
[25] Leong E S P, Liu Y J, Deng J, Fong Y T, Zhang N, Wu S J and Teng J H 2014 *Nanoscale* **6** 11106–11
[26] Reilly T H III, Chang S-H, Corbman J D, Schatz G C and Rowlen K L 2007 *J. Phys. Chem.* C **111** 1689–94
[27] Chu Y, Banaee M G and Crozier K B 2010 *ACS Nano* **4** 2804–10
[28] Wang M S, Zhao C L, Miao X Y, Zhao Y H, Rufo J, Liu Y J, Huang T J and Zheng Y B 2015 *Small* **11** 4423–44
[29] Si G Y, Zhao Y H, Liu H, Teo S L, Zhang M S, Huang T J, Danner A J and Teng J H 2011 *Appl. Phys. Lett.* **99** 033105
[30] Palik E D 1985 *Handbook of Optical Constants of Solids* (Orlando, USA: Academic Press)
[31] Duan H, Hu H, Kumar K, Shen Z and Yang J K W 2011 *ACS Nano* **5** 7593–600
[32] Wang Y M, Lu L X, Srinivasan B M, Asbahi M, Zhang Y W and Yang J K W 2015 *Sci. Rep.* **5** 9654
[33] Cui B and Veres T 2007 *Microelectron. Eng.* **84** 1544–7
[34] de Waele R, Burgos S P, Polman A and Atwater H A 2009 *Nano Lett.* **9** 2832–7
[35] Ghaemi H F, Thio T, Grupp D E, Ebbesen T W and Lezec H J 1998 *Phys. Rev.* B **58** 6779–82